APL Materials

In situ observation of medium range ordering and crystallization of amorphous TiO_2 ultrathin films grown by atomic layer deposition

Cite as: APL Mater. **11**, 011102 (2023); https://doi.org/10.1063/5.0130918
Submitted: 16 October 2022 • Accepted: 08 December 2022 • Published Online: 03 January 2023

Mehrdad Abbasi, Yutao Dong, Jun Meng, et al.

In situ observation of medium range ordering and crystallization of amorphous TiO_2 ultrathin films grown by atomic layer deposition

Cite as: APL Mater. 11, 011102 (2023); doi: 10.1063/5.0130918
Submitted: 16 October 2022 • Accepted: 8 December 2022 •
Published Online: 3 January 2023

Mehrdad Abbasi,[1,a] Yutao Dong,[2] Jun Meng,[2] Dane Morgan,[2] Xudong Wang,[2] and Jinwoo Hwang[1,a]

AFFILIATIONS

[1] Department of Materials Science and Engineering, The Ohio State University, Columbus, Ohio 43210, USA
[2] Department of Materials Science and Engineering, University of Wisconsin-Madison, Madison, Wisconsin 53706, USA

[a] **Authors to whom correspondence should be addressed:** abbasigharacheh.1@buckeyemail.osu.edu and hwang.458@osu.edu

ABSTRACT

The evolution of medium range ordering (MRO) and crystallization behavior of amorphous TiO_2 films grown by atomic layer deposition (ALD) were studied using *in situ* four-dimensional scanning transmission electron microscopy. The films remain fully amorphous when grown at 120 °C or below, but they start showing crystallization of anatase phases when grown at 140 °C or above. The degree of MRO increases as a function of temperature and maximizes at 140 °C when crystallization starts to occur, which suggests that crystallization prerequires the development of nanoscale MRO that serves as the site of nucleation. *In situ* annealing of amorphous TiO_2 films grown at 80 °C shows enhancement of MRO but limited number of nucleation, which suggests that post-annealing develops only a small portion of MRO into crystal nuclei. The MRO regions that do not develop into crystals undergo structural relaxation instead, which provides insights into the critical size and degree of ordering and the stability of certain MRO types at different temperatures. In addition, crystallographic defects were observed within crystal phases, which likely negate corrosion resistance of the film. Our result highlights the importance of understanding and controlling MRO for optimizing ALD-grown amorphous films for next-generation functional devices and renewable energy applications.

I. INTRODUCTION

Storing solar energy as "solar fuels" has recently drawn a significant attention for reliable and sustainable energy production and distribution.[1–3] For instance, hydrogen can be produced from water using solar energy via photoelectrochemical water-splitting (PEC) process, where a photoanode absorbs photons from the sunlight and generates charge carriers to electrolyze water into hydrogen and oxygen.[4,5] While still at the laboratory scale, several materials have been demonstrated for use in photoanodes in PEC cells.[6–8] One good candidate is silicon photo-anode, which has the benefit of low manufacturing cost as well as good light absorption.[9,10] However, the corrosion of Si photoanode in alkaline environment has been reported to be an obstacle for durability and efficiency of PEC cells over time.[11,12] To overcome this issue, amorphous TiO_2 (a-TiO_2) grown by atomic layer deposition (ALD) that is optically transparent and electrically conductive has been introduced as an effective protective layer for Si photoanodes.[13–15] ALD can grow an ultrathin, pinhole free conformal a-TiO_2 film on the silicon using binary reactants of $TiCl_4$ and H_2O.[16] a-TiO_2 film can be sequentially grown by ALD process based on the following overall reaction [Eq. (1)]:[17,18]

$$TiCl_4(g) + H_2O(g) \rightarrow TiO_2(s) + HCl(g). \quad (1)$$

In general, two half reactions occur during ALD growth of a-TiO_2 form $TiCl_4$ and H_2O on a substrate,[19,20]

$$n(-OH)(s) + TiCl_4(g) \rightarrow (-O-)_nTiCl_{4-n}(s) + nHCl(g), \quad (2)$$

$$(-O-)_nTiCl_{4-n}(s) + (4-n)H_2O(g) \rightarrow (-O-)_nTi(OH)_{4-n}(s) + (4-n)HCl(g), \quad (3)$$

where the $TiCl_4$ precursor reacts with –OH groups on the substrate surface [Eq. (2)], and then the water reacts with absorbed $TiCl_x$ groups, which results in a TiO_2 network and bonded –OH groups [Eq. (3)]. In addition, the reaction between the bonded –OH groups occurs to form purer a-TiO_2,

$$\mathrm{Ti(-OH)-O-Ti(OH)}(s) \rightarrow \mathrm{Ti(-O-)_2}(s) + \mathrm{H_2O}(g). \quad (4)$$

However, unreacted species (impurities) could remain during ALD process as temperature plays a key role in the completion of reactions.[21] Hence, prolonged water exposure or post-deposition annealing was suggested to increase film purity.[22] Meanwhile, an elevated temperature during ALD growth or post-deposition annealing may lead to the formation of crystalline particles within the film.[23,24] It was also reported that protectiveness of a-TiO_2 film was impaired due to the presence of secondary phase particles formed during growth process in the amorphous matrix.[25] Moreover, it was found that the ALD TiO_2 film showed inferior protection when the film is crystallized. This was attributed to the presence of preferential conduction paths due to the existence of grain boundaries and defects in the crystalline film.[26] Furthermore, several other works[27–30] have shown that crystalline phases in amorphous ALD-grown TiO_2 films can substantially negate the protection function of the layer and reduce the lifetime of the electrode. While these studies highlight the importance of understanding the formation of crystalline phases in a-TiO_2 films, many important questions still need to be addressed, including (i) what type of structural evolution in the amorphous structure could lead to crystallization, (ii) what kind of nucleation and growth process the crystallization involves, (iii) how the crystallization process is affected by the growth condition and post-processing (such as heat treatment), (iv) what is the dominant structure of the nuclei as well as the fully grown crystal phases, and (v) what kind of defects those phases may have. Answering these questions will directly benefit the understanding of structural change prior to crystalline nucleation and help optimize the synthesis conditions for having uniformly amorphous films to substantially increase the stability and lifetime of the PEC system.

In this study, we use quantitative analysis of nano-diffraction patterns acquired using 4-dimensional scanning transmission electron microscopy (4D-STEM) as well as high resolution STEM to investigate the details of the structure of ALD-grown TiO_2 films to deliver answers to the important questions stated above. Especially, we focus on the characteristics and evolution of medium range ordering (MRO), which constitutes structural heterogeneity at the nanometer scale.[31,32] In general, MRO refers to nanoscale volumes in amorphous materials where the atoms are relatively more ordered than other regions.[33] Spatial distribution of these MRO regions will lead to "fluctuation" of the degree of ordering, which has been measured using a diffraction technique known as fluctuation electron microscopy (FEM).[34,35] FEM measures the intensity variance, V, among diffraction intensities from local regions of the sample as a measure of structural fluctuation. V should increase when the degree of MRO (or nanoscale heterogeneity) increases, since the MRO regions should diffract the incoming electrons more strongly than the disordered regions. V is typically measured as a function of the scattering vector magnitude, k, which also provides important information about the internal structure of MRO (i.e., type of the MRO).[36,37] FEM was previously used to study crystallization in amorphous materials. For example, Lee[38] studied nucleation and growth of crystalline phases in chalcogenide Ag/In-incorporated Sb_2Te and reported higher structural heterogeneity at the areas affected by laser annealing. More recently, Rezikyan and Moore[39] showed the change in MRO as a function of annealing temperature in SiO_2 glass containing a low content of TiO_2. In addition to V analysis, we use high resolution STEM to observe the atomic structure of crystalline particles as well as angular correlation analysis of nano-diffractions from 4D-STEM[40–42] to reveal the dominant symmetry of MRO. The combined use of these techniques on samples controlled with ex situ (ALD processing) and *in situ* (post-annealing) conditions provides information about the stages of MRO evolution and formation of the dominant crystalline phase as a function of ALD growth and post-annealing temperatures. Our result shows that the degree of MRO increases as a function of the ALD growth temperature, which eventually leads to the nucleation of crystalline anatase phases at the growth temperature of 140 °C or above, indicating that the local MRO regions are likely the sites of nucleation. High resolution STEM images reveal crystallographic defects within the crystal phases, which should reduce the corrosion resistance of the film. Post-*in situ* annealing of the films also leads to enhancement of MRO, but unlike the case of growth temperature, only a limited number of nucleation of crystalline phases were observed, which suggests that only a small portion of MRO domains develops into nuclei beyond the critical size in post-annealing. The MRO regions that do not develop into crystal instead go through structural relaxation, possibly suggesting that MRO reduces its configurational energy at certain temperatures. Overall, the TiO_2 films remain fully amorphous when the ALD growth temperature remained below 120 °C and when the post-annealing temperature was below 400 °C. Our present results reveal details of the structure and evolution of TiO_2 amorphous films in ALD synthesis of these films, which will provide important guidance for further development and optimization of PEC systems with long lifetime and high efficiency, as well as ALD synthesis for functional and energy applications in general.

II. EXPERIMENTAL METHODS

A. Amorphous TiO_2 films

Freestanding amorphous TiO_2 was prepared by atomic layer deposition (ALD) on a thin polyvinylpyrrolidone (PVP) water-soluble sacrificial layer on Si wafer. The thin PVP layer was fabricated by a spin-coating method with the PVP aqueous solution dropped onto silicon wafer at 3000 rpm with 30 s. The PVP aqueous solution was made by dissolving PVP powder (molecular weight ~35 000) in DI H_2O (18.2 MΩ) with 2 wt. % concentration. Amorphous TiO_2 was deposited onto fresh PVP layer coated Si wafer at various temperatures (100 °C, 120 °C, 140 °C, 160 °C) in a home-made ALD system. The PVP/Si substrate was loaded on a quartz boat and placed 4 cm away from the precursor inlet nozzle. N_2 gas with a flow rate of 40 sccm was introduced into the chamber as the carrier gas, which generated a base pressure of 720 mTorr. During the ALD process, the chamber temperature was set at 100 °C, 120 °C, 140 °C, and 160 °C. Titanium tetrachloride ($TiCl_4$, Sigma-Aldrich, 99.9%) and H_2O vapors were pulsed into the chamber alternatively with an exposure time of 0.5 s, respectively, and separated by 60 s N_2 purging. Therefore, one ALD cycle involves 0.5 s of H_2O pulse +60 s

of N_2 purging +0.5 s of $TiCl_4$ pulse +60 s of N_2 purging and continuously 200 cycles were grown onto PVP/Si substrate. To acquire freestanding TiO_2 amorphous films, wafer samples were immersed in de-ionized (DI) H_2O to dissolve PVP at room temperature for 1 h to fully release TiO_2 film to be transferred to TEM grids for characterizations. Figure 1(a) shows the a-TiO_2 film on TEM grid. The thickness of the film was measured using the cross-sectional STEM image of the film, which consistently showed 15 nm for all samples that we observed. An example of the film cross section is shown in Fig. S1.

Post-annealing of the film was performed *in situ* using a heating TEM holder from DENS Solutions. This double tilt holder uses a MEMS type heating chip [Fig. 1(b)] patterned on SiN membrane, which ensures fast annealing and cooling up to 1200 °C/sec and high temperature precision (±5%). a-TiO_2 films were placed on the chip area, and the electron scattering signals (both for diffraction and imaging) were recorded through the premade circular holes on the SiN membrane. The samples were then annealed up to around 400 °C, as the formation of crystalline phases from amorphous matrix is previously reported at that temperature.[43] Each heating cycle included rapid heating to a target temperature in 1 s, holding at that temperature for 15 min, and rapid cooling to room temperature in 1 s.

B. STEM Characterization

4D-STEM acquires nano-diffraction patterns from all individual probe positions while the probe scans over the sample[34] [Fig. 1(c)]. We performed 4D-STEM using a Thermofisher Scientific Themis Z STEM operated at 200 kV and equipped with an Electron Microscopy Pixel Array Detector (EMPAD) with 32 bit dynamic range, 1 kHz readout speed, and 4 ms probe dwell time.[44]

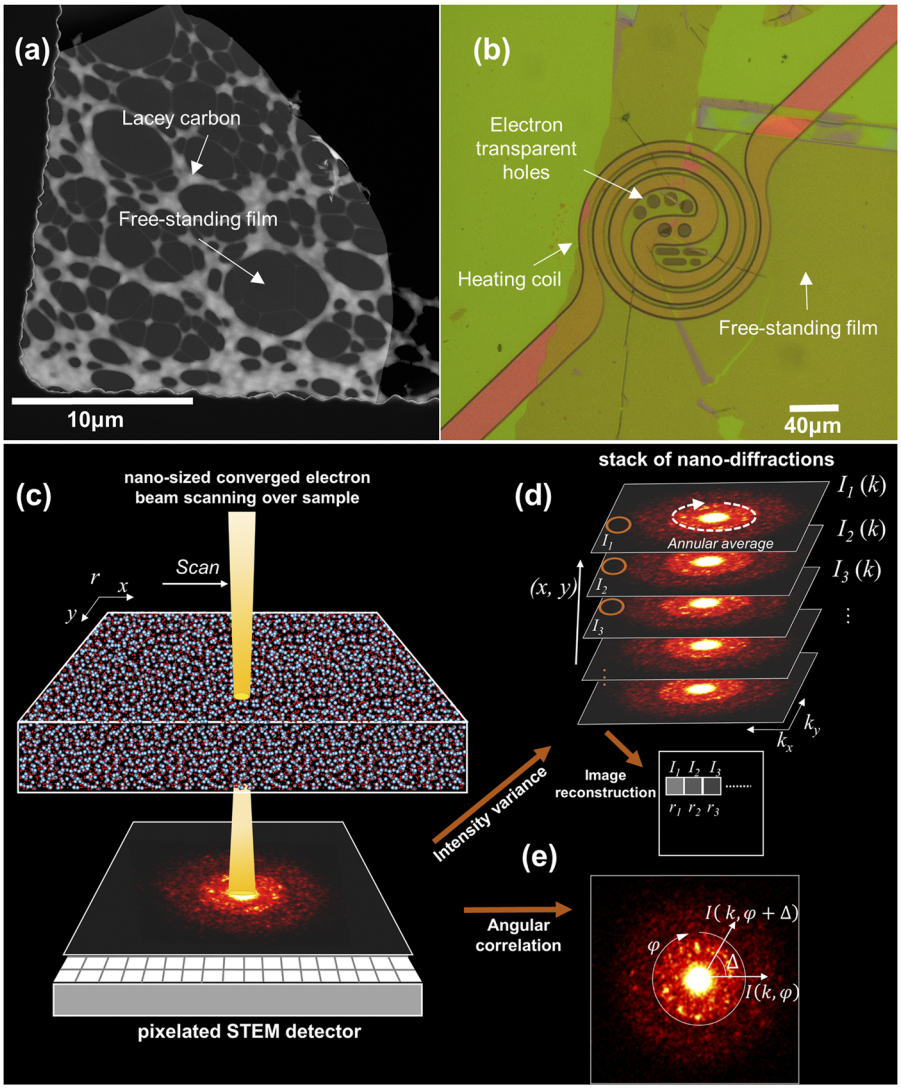

FIG. 1. (a) An ALD-grown a-TiO_2 film on a lacey carbon TEM grid. (b) Free-standing a-TiO_2 film placed on the heating area of the *in situ* heating chip. (c) Schematic of 4D-STEM, (d) intensity variance analysis and virtual image reconstruction, and (e) and notations for angular correlation analysis from the 4D-STEM data.

The electron probe with a size (R) of 1.4 nm was formed using a 10 μm C_2 aperture and a convergence angle of 2 mrad. The probe was scanned over the sample area with 256 × 256 square grid positions, which corresponds to 184 × 184 nm^2 in length. This ensures that the probe positions are spatially oversampled and no area on the sample surface was left uncovered by the probe. The scan was done over multiple areas of each sample and the resulting data, such as intensity variance and angular correlation functions, were averaged over the areas to ensure statistical significance.

An example of nano-diffraction patterns from 4D-STEM are shown in Fig. 1(c). Unlike in the case of large area diffraction patterns from an amorphous sample where multiple "fuzzy" rings are typically observed, the nano-diffraction patterns from amorphous samples show small, bright speckles that include diffraction signals from local regions. If so, the diffraction speckles from MRO structure should be more dominant over other statistically insignificant (or random) diffraction signals. Extracting the dominant MRO signal from the diffraction intensity can be done by calculating the normalized variance, V,[35]

$$V(k,R) = \frac{\langle I^2(r,k,R)\rangle_r}{\langle I(r,k,R)\rangle_r^2} - 1, \tag{5}$$

where I is the diffraction intensity acquired by annular averaging each nano-diffraction pattern [Fig. 1(d)], r is the position of the probe in (x, y) real space, and $< >_r$ represents spatial averaging over r. The rationale is that when significant MRO is present, the diffraction from the MRO will appear or disappear depending on their spatial and orientation distribution (i.e., whether they are aligned along the Bragg angle or not), which will make V increase. On the other hand, a low degree of MRO will show low V. This way, V can be used as a relative measure of the degree of MRO or the degree of structural fluctuation at the length scale of the measurement (i.e., probe size) due to the presence of MRO. More quantitatively, V is related to "many-body" correlation function, which is more likely related to the structure at the MRO scale, as opposed to I—which only shows atomic pair information (2-body correlation) that is averaged over the entire probed volume and therefore lost information about the nanoscale heterogeneity.[45,46] Since I is already a function of k, V is naturally a function of k as well. Like in any diffraction measurement, k is inverse of the "interplanar spacing" within the ordering (which represents the type of ordering). V is maximized when R is close to the size of MRO,[37,47] which is typically about 1 to a few nanometers in size.[48] We used R = 1.4 nm in this work.

Same nano-diffraction patterns from 4D-STEM were also used to calculate angular correlation function, $C_k(\Delta)$,[40]

$$c_k(\Delta) = \frac{\langle I(k,\varphi)I(k,\varphi+\Delta)\rangle_\varphi - \langle I(k,\varphi)\rangle_\varphi^2}{\langle I(k,\varphi)\rangle_\varphi^2} - 1, \tag{6}$$

where Δ is the difference between two scattering vectors and $\langle\rangle_\varphi$ represents averaging over the annular direction [Fig. 1(e)]. $C_k(\Delta)$ reveals the angular correlation between two diffraction speckles at the same k and therefore it can reveal any statistically significant rotational symmetry "hidden" in nano-diffraction patterns. This complements the information from V, where the angular correlation information is lost due to averaging of I over the annular direction to obtain $I(k)$. Due to Friedel symmetry in diffraction,[49] 2-fold signal is expected to rise when there is any set of atomic planes within the atomic structure (even though they are not well-ordered like in crystals). Recent angular correlation studies also revealed that MRO in amorphous materials can show higher structural symmetries, represented by 4- or 6-fold signals in $C_k(\Delta)$.[50] It is important to note that both V and $C_k(\Delta)$ require a consistent TEM sample thickness to avoid any artifact in the data. As mentioned above, the film thicknesses were consistently 15 nm for all films that we examined.

In addition, MRO and crystal particles were directly observed in the dark field (DF) images with 256 × 256 pixels that are virtually reconstructed from the 4D-STEM data for all k.[51] This is based on the fact, that, since the nano-diffraction intensities (I) were acquired in 4D, i.e., 2D real space, $r(x, y)$ plus 2D reciprocal space, $k(k_x, k_y)$, the real space image (r_1, r_2, r_3, …) of the sample can be digitally reconstructed using any (k_x, k_y) value [Fig. 1(d)]. For example, if a k vector outside of the zero (transmitted) beam is used for the reconstruction, then the resulting image is analogous to DF images acquired using a small objective aperture in a conventional TEM setting. Since MROs appear brighter in DF images, the MRO regions were identified by setting an intensity threshold, then the average size of MRO was calculated for each k.[34] In addition, the details of the crystal structure and defects within each crystalline particle were acquired using high resolution STEM with a probe semi-convergence angle of 18 mrad at 300 kV. Diffraction contrast from the crystal phases were also imaged using the low angle annular DF (LAADF) mode in STEM.

III. RESULTS AND DISCUSSION

A. Effect of ALD growth temperature

First, we show the effect of ALD growth temperature on the evolution of MRO and nucleation of crystalline phases in a-TiO_2. Figure 2 shows the example DF images reconstructed from the 4D-STEM data using a k range between 4.5 and 5.5 nm^{-1} for films grown at different temperatures. At 100 and 120 °C [Figs. 2(a) and 2(b), respectively], the films appear to be fully amorphous without the presence of any crystalline phase particle as evidenced by the averaged nano-diffraction pattern from the area in the inset (white outlined) showing amorphous rings. In these images, there are areas showing nanoscale regions that are relatively bright (e.g., regions indicated with yellow arrows). These bright spots correspond to nano-volumes that generate relatively strong diffraction signals; in other words, they are the MRO regions that diffract toward the particular k that was used to reconstruct the DF image. However, they do not represent all the MRO regions present in the area, since the image only shows MRO regions diffracting toward that particular k vector. The individual diffraction patterns shown in the insets with yellow outlines in Figs. 2(a) and 2(b) were from the MRO areas, and they show relatively strong diffraction speckles, which indicates a higher degree of ordering in that area although the overall structure is still disordered and cannot be considered as a crystalline phase. On the other hand, in the film grown at higher temperature, 140 °C, a small number of crystalline particles nucleates from the amorphous matrix with a strong diffraction intensity as shown in Fig. 2(c). This crystal diffraction pattern matches with the (010) oriented anatase phase. The particle also has more clearly defined boundary against the surrounding regions, which is

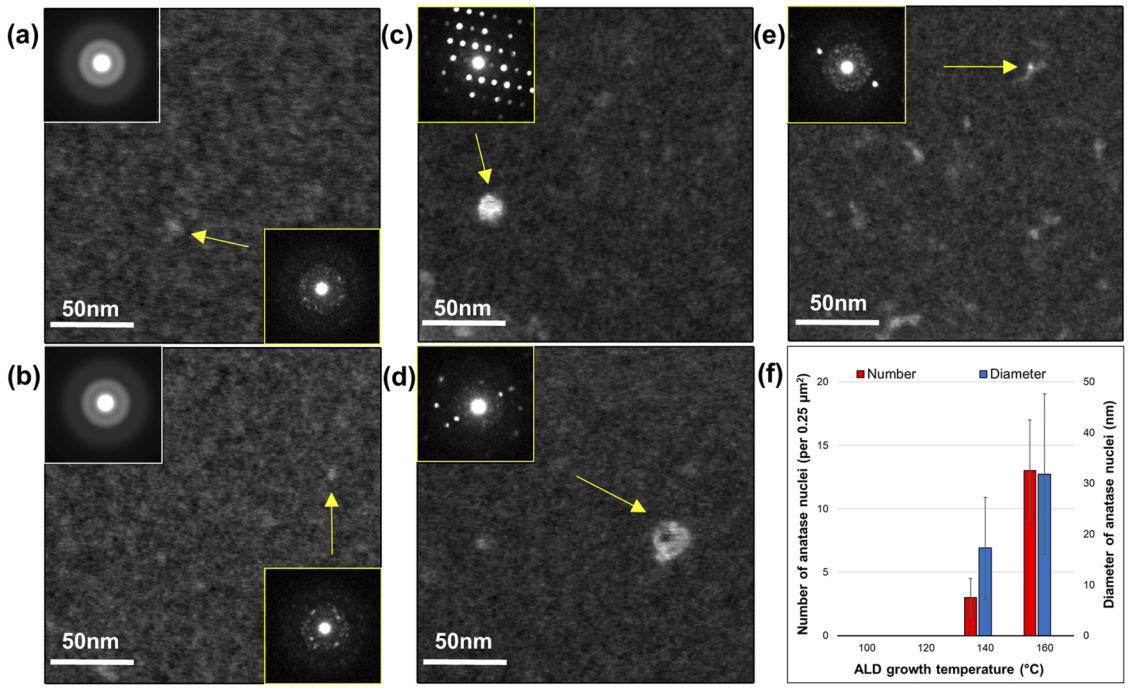

FIG. 2. Reconstructed DF images from a sampling area of a-TiO_2 films ALD-grown at (a) 100 °C, (b) 120 °C, (c) 140 °C, and (d and e) 160 °C. The inset within the white outline shows the diffraction pattern averaged over the entire area, and the inset within the yellow outline shows the pattern acquired from the area indicated by the yellow arrow. (f) Average number and size of nanocrystalline particles observed in the films grown at different temperatures.

different from the case of the MRO shown in Fig. 2(a). Similarly, the nanocrystalline particles with strong nano-diffraction patterns are also observed for the film grown at 160 °C as one example is shown in Fig. 2(d). Moreover, Fig. 2(e) shows an example of a very small (~5 nm in size) nanocrystalline particle (yellow arrow) in the film grown at 160 °C. Interestingly, this particle, which shows a strong nano-diffraction pattern (inset), formed right adjacent to a MRO domain (which is the relatively bright amorphous region), suggesting that MRO domains can be possible sites for crystalline nucleation, although other potential nucleation sites (e.g., surfaces or regions with impurities) cannot be ruled out. In general, as shown in Fig. 2(f), both the size and number of these nanocrystals increase in the film grown at 160 °C compared to the one grown at 140 °C, suggesting crystalline nucleation accelerates when the film is grown at 160 °C.

The results shown in Fig. 2 suggest that there may be an inherent relationship between MRO and crystallization in these a-TiO_2 films. To understand how the degree of MRO changes as a function of the growth temperature and potentially relates to crystal nucleation in a-TiO_2 films, we calculated V from 4D-STEM nano-diffraction patterns using Eq. (1). The results are shown in Fig. 3(a). Different colors represent the V's for samples grown at different temperatures, and the shade around each line represents the range of experimental uncertainty (±standard deviation of mean[52]). V from all temperatures show a broad peak at ~3.2 nm^{-1}, and the second peak at around 5 nm^{-1}. For comparison, the diffraction peak positions of the three known crystalline phases of TiO_2 (anatase, brookite, and Rutile) are plotted as vertical lines at the bottom of the graph in Fig. 3(a).[53–55] The highest peaks of all three known crystal phases are within the k range of the first peak, indicating that MRO may inherently resemble the structure of crystalline phases, which is also consistent with the finding from other amorphous systems, such as amorphous silicon, metallic glasses, and polymers (e.g., Refs. 37, 56–58). More importantly, the amplitude of V changes significantly as the growth temperature changes. The 100 °C data show the lowest V, but it gradually increases and reaches a maximum at 140 °C, which is the temperature that we first observed for a small number of crystalline nuclei. This further suggests that the regions with high degree of MRO can evolve into crystalline nuclei as the temperature increases. In addition, V slightly decreased at 160 °C when several nuclei formed within the film. This implies that, as nucleation accelerates and more nuclei form, regions with higher degree of MRO turn into nanocrystals, thus we are left with the amorphous regions with slightly lower degree of MRO where the V at 160 °C was measured. Moreover, we also observe a trend in the peak positions in $V(k)$, both in the first and second peaks, which is that the peaks move toward higher k as the growth temperature increases. The position of the first peak is at ~3 nm^{-1} for the 100 °C sample, but it gradually moves to ~3.3 nm^{-1} at higher temperatures. The same trend was seen in the second peak position, which moves from ~5 to 5.3 nm^{-1}. This indicates that interplanar spacing within the MRO (which produces the diffraction signal) becomes smaller as the internal ordering within the MRO becomes more well-developed at higher temperatures.

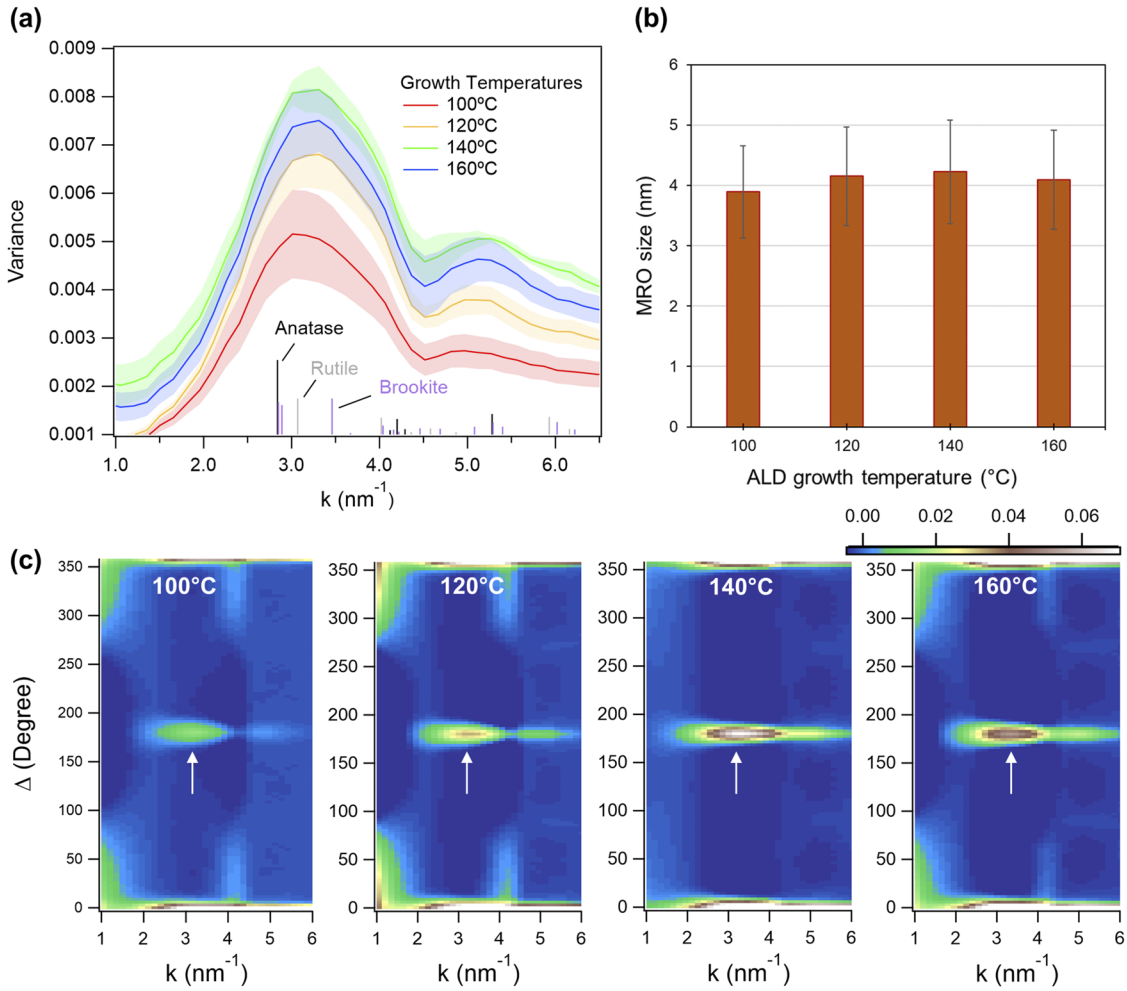

FIG. 3. (a) Intensity variance plots of amorphous TiO_2 films grown at different ALD temperatures. The shades indicate the experimental uncertainty of the measurement, and the diffraction peak positions of the known TiO_2 crystal phases are also indicated for comparison. (b) Averaged MRO size at $k \sim 3.2\ nm^{-1}$ for films grown at different ALD temperatures. (c) Averaged angular correlation function, $C_k(\Delta)$, of the a-TiO_2 films grown at different temperatures.

We directly measured the MRO size by applying an intensity threshold value to the dark field images reconstructed from the 4D-STEM data for all k using the method described in Sec. II. The measured MRO size, average ±standard deviation, at $k \sim 3.2\ nm^{-1}$ is plotted in Fig. 3(b) for films grown at different temperatures (note that the measured MRO size can be slightly overestimated since it convolutes the probe size[34]). As shown in the figure, the change in MRO size by the ALD growth temperature is within the experimental uncertainty (error bar range). Despite the statistical insignificance of the change, the average MRO size has a subtle trend that shows the maximum MRO size at 140 °C, which may correspond to the trend shown in the variance data in Fig. 3(a). Regardless, the fact that the MRO size showed very little change suggests that the change in variance [Fig. 3(a)] is likely due to change in the atomic arrangement (or structural symmetries) within the MRO rather than change in the MRO sizes.

To understand the changes in structural symmetry within MRO at different growth temperatures, same 4D-STEM nano-diffraction data were used to calculate the angular correlation function [Eq. (6)], $C_k(\Delta)$, Fig. 3(c) shows the averaged $C_k(\Delta)$ plots from each film grown at different temperatures. Each plot presents $C_k(\Delta)$, which is the color scale, as a function of the in-plane rotation angle, Δ (y-axis), and k (x-axis). All $C_k(\Delta)$ plots show a broad peak at $\Delta \sim 180°$ (indicated with white arrows), which represents 2-fold symmetry in the diffraction pattern, at around $k \sim 3.2\ nm^{-1}$, which corresponds to the peak positions observed in $V(k)$ shown in Fig. 3(a). Previous works have shown that disordered network of a-TiO_2 consists of mostly TiO_6 octahedrons.[59,60] MRO could be considered as more aligned arrangements of octahedrons compared to their random arrangement in the amorphous matrix, which could lead to appearance of 2-fold rotational symmetry in $C_k(\Delta)$. Considering the arrangement of octahedrons in TiO_2 crystalline

phases shown in Fig. S2, it can be suggested that MRO in a-TiO_2 could resemble brookite, anatase, or rutile phases to some extent where 2-fold symmetry is more dominant. For example, the similarity between a-TiO_2 and brookite phase was previously reported by Petkov *et al.*[61] It is seen in Fig. 3(c) that the intensity of the 2-fold peak in $C_k(\Delta)$ changes as a function of the growth temperature with exactly the same trend as $V(k)$ shown in Fig. 3(a). The $C_k(\Delta)$ data therefore suggest that 2-fold symmetry is the dominant structural symmetry in MRO that also gives rise to the peaks in $V(k)$ and that the degree of 2-fold symmetry is closely tied to the evolution of MRO. Enhancement of the 2-fold symmetry may indicate that the polyhedrons rearrange themselves and develop into a more well-ordered nanoscale network (which is essentially MRO) at higher growth temperatures, which may eventually further evolve to crystalline nuclei.

B. Crystalline nuclei formed during ALD growth

The presence of crystalline particle in a-TiO_2 films could negatively affect the film protection ability since the particles can be more easily attacked by hydroxyl groups in PEC cell, resulting in localized corrosion.[25] The atomic structure of nanocrystalline particles grown during ALD process was investigated using high resolution STEM imaging, and the details of crystalline particle growth were observed via *in situ* annealing in STEM. Figure 4(a) shows an example crystalline TiO_2 particle observed in the a-TiO_2 film grown at 160 °C. The particles are generally spherically shaped, and the average size of the particles observed was ~36 nm [Fig. 2(f)]. A detailed view shows that the atomic structure [Fig. 4(b)] matches the structure of the [110] orientation of anatase phase, which is consistent with previous reports.[30,43] Some crystallographic defects were also observed, such as the stacking faults seen in Fig. 4(b). These defects may serve as preferential sites for diffusion of ions and corrosion during the operation of PEC cell. In addition, the sharp interface between the crystal and amorphous matrix [Figs. 4(c) and 4(d)] could also serve as a preferential diffusion pathway for corrosive ions. When the sample was *in situ* annealed at 400 °C, the anatase particle showed further growth, extending its crystal structure into the amorphous region within a few seconds [Fig. 4(e)]. Figure 4(f) shows a low magnification image of a completely crystallized film, which reveals the details of the microstructure, including grain boundaries as well as the strain within the crystal phase evidenced by the bend contours. As mentioned above, these crystallographic defects can also be pathways to electrolyte and can cause corrosion.[26] The *in situ* annealing experiment therefore shows that the crystal phases that are already present in the film during growth can rapidly grow above certain temperatures in post-annealing, creating crystallographic defects and interfaces that are detrimental for film properties. Based

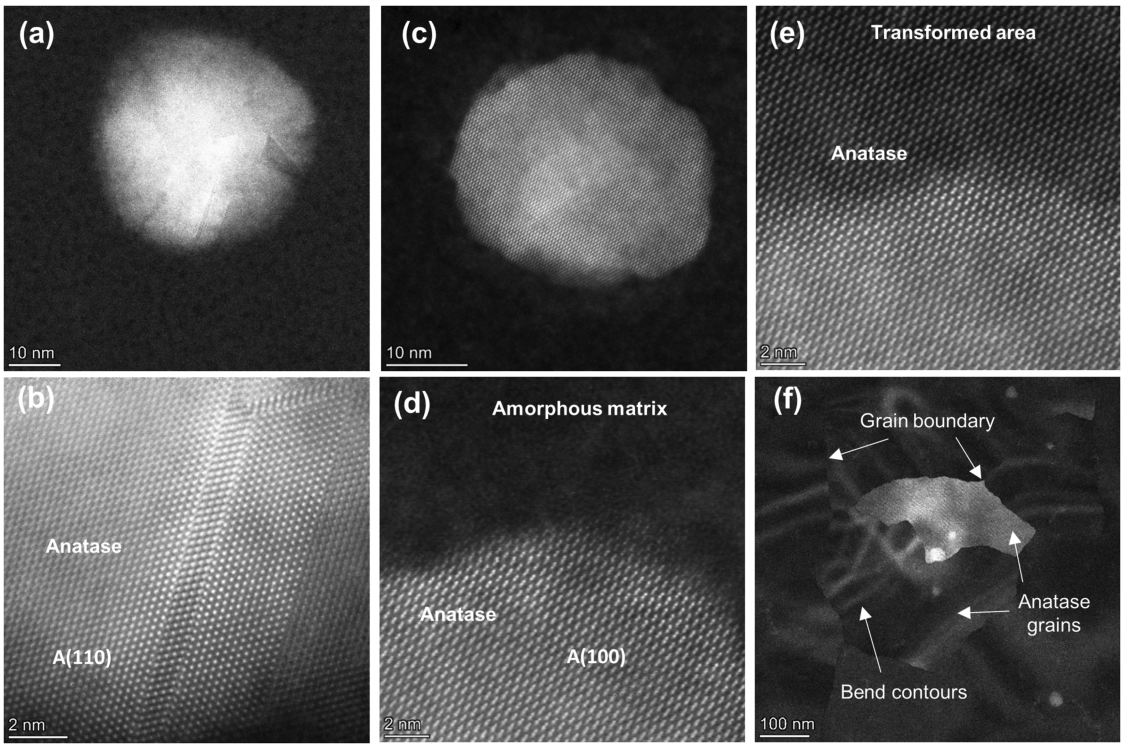

FIG. 4. (a) High resolution STEM image of a nanocrystal in a-TiO_2 film grown at 160 °C. (b) Details of the atomic structure and defects within the anatase TiO_2 nanoparticle shown in (a). (c) A smaller nanocrystal in the film grown at 160 °C. (d) The anatase particle before *in situ* annealing and (e) a few seconds after *in situ* annealing at 400 °C. The crystallinity extends to the amorphous region after the growth. (f) Lower magnification image of the crystal grown after *in situ* annealing.

on these results, we conclude that ALD growth at lower temperatures (below 120 °C) may be preferred to avoid any crystallization or further growth of crystal phases.

C. Post-annealing of fully amorphous a-TiO_2

Next, the effect of post-thermal annealing on fully amorphous films (grown at 80 °C) was studied using *in situ* 4D-STEM. Post-treatment annealing is generally known to enhance the structural integrity and chemical purity of ALD-grown films. For example, the bounded –OH groups could react with each other via the process shown in Eq. (4) during annealing, which could result in purer a-TiO_2 films. However, the possibility of formation of crystalline phases significantly increases during annealing. Hence, we have investigated the effect of annealing on the MRO and crystallization of an a-TiO_2 film that was originally fully amorphous after the ALD growth at 80 °C. Figures 5(a)–5(h) show LAADF STEM images of films *in situ* annealed at different temperatures. First, before annealing, the film appears to be fully amorphous at room temperature, as shown in Fig. 5(a). When annealed at 300 °C and 400 °C [Figs. 5(b) and 5(c)], no crystallization is seen, but the bright spots in the amorphous film appear to be more prominent, which indicates the development of MRO domains. The first crystalline particle in the film was observed at 415 °C as shown in Fig. 5(d). The particles subsequently grew to a few hundred nanometers in size within a few minutes at 430 °C [Fig. 5(e)]. The diffraction pattern from the crystal matches with the 011 orientation of anatase phase [inset in Fig. 5(e)]. At 500 °C, the entire film was crystallized, as shown in Fig. 5(f). The images from a larger field of view [Fig. 5(g)] revealed that only a very small number of crystal phases have nucleated from the amorphous film at 430 °C. The limited number of nucleation here is different from what was observed in the case of growth temperature study, where we saw abundant nucleation sites (Sec. III A). The approximate number density of crystal particle in Fig. 5(g) is ~0.016 μm^{-2}, which is much lower than what we observed in the case of growth temperature study [e.g., ~12 μm^{-2} when grown at 140 °C, as shown in Fig. 2(f)]. Further growth of those particles eventually led to crystallization of the entire film at 500 °C [Fig. 5(h)], with very limited nucleation of crystals at other locations. Based on this result, it can be concluded that the high degree of MRO is more likely due to chemical reaction during the growth at higher temperatures (which lasted for about 8 h in our case), and the film can easily evolve into crystallization (because high MRO means more abundant nucleation sites) when post-annealed. On the other hand, the films grown at a low temperature (e.g., 80 °C) have low degree of MRO, which means that even post-annealing at high temperature would not lead to abundant nucleation since the nucleation sites were already limited by the low degree of MRO. This again emphasizes the importance of using the low growth temperatures to prevent any nucleation.

To observe the change in degree of MRO during *in situ* annealing, $V(k)$ was calculated from the 4D-STEM data acquired from the sample at different temperatures during annealing [Fig. 6(a)]. The original sample (as-grown, before annealing) was grown at 80 °C, and it shows a low V, lower than that of V from the film grown at 100 °C shown in Fig. 3(a). When annealed at 300 °C and 400 °C, the V increased significantly, up to ~0.0085 (note that there is still no crystallization at this point as shown in Fig. 5). This maximum level of V shows a quantitative match to the maximum V shown in the growth temperature study shown in Fig. 3(a), which suggests that the degree of MRO can reach a "saturation point" before crystallization, regardless of whether the MRO forms during growth or via post-annealing. However, there is a key difference between the data presented in Figs. 3(a) and 6(a). As mentioned earlier, the peak

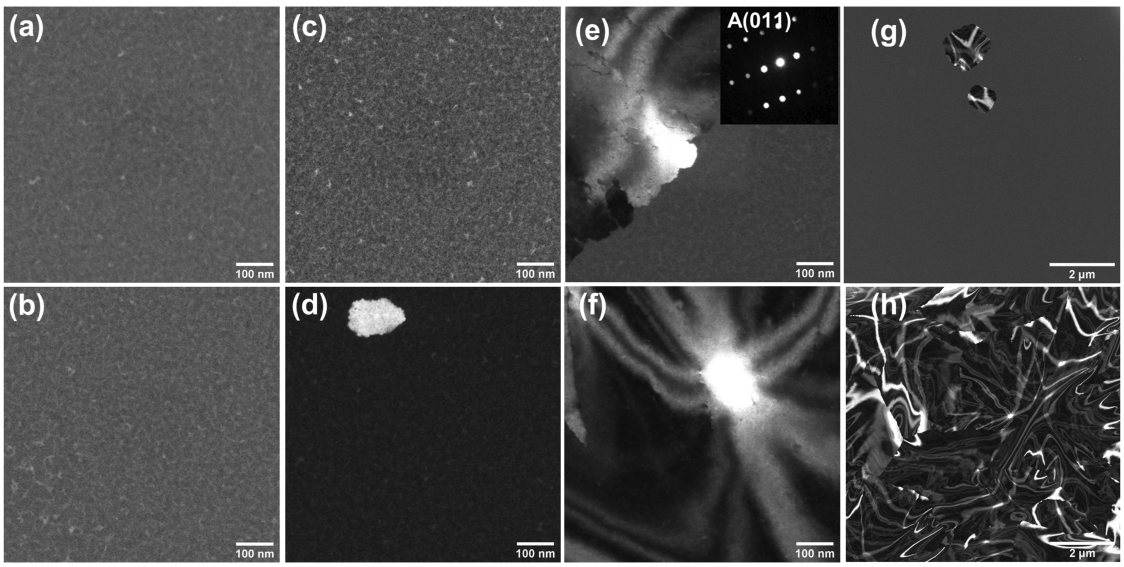

FIG. 5. STEM images of fully amorphous TiO_2 films at (a) room temperature, after *in situ* annealing at (b) 300 °C, (c) 400 °C, (d) 415 °C, (e) 430 °C, and (f) 500 °C as well as lower magnification images of films annealed at (g) 430 °C and (h) 500 °C.

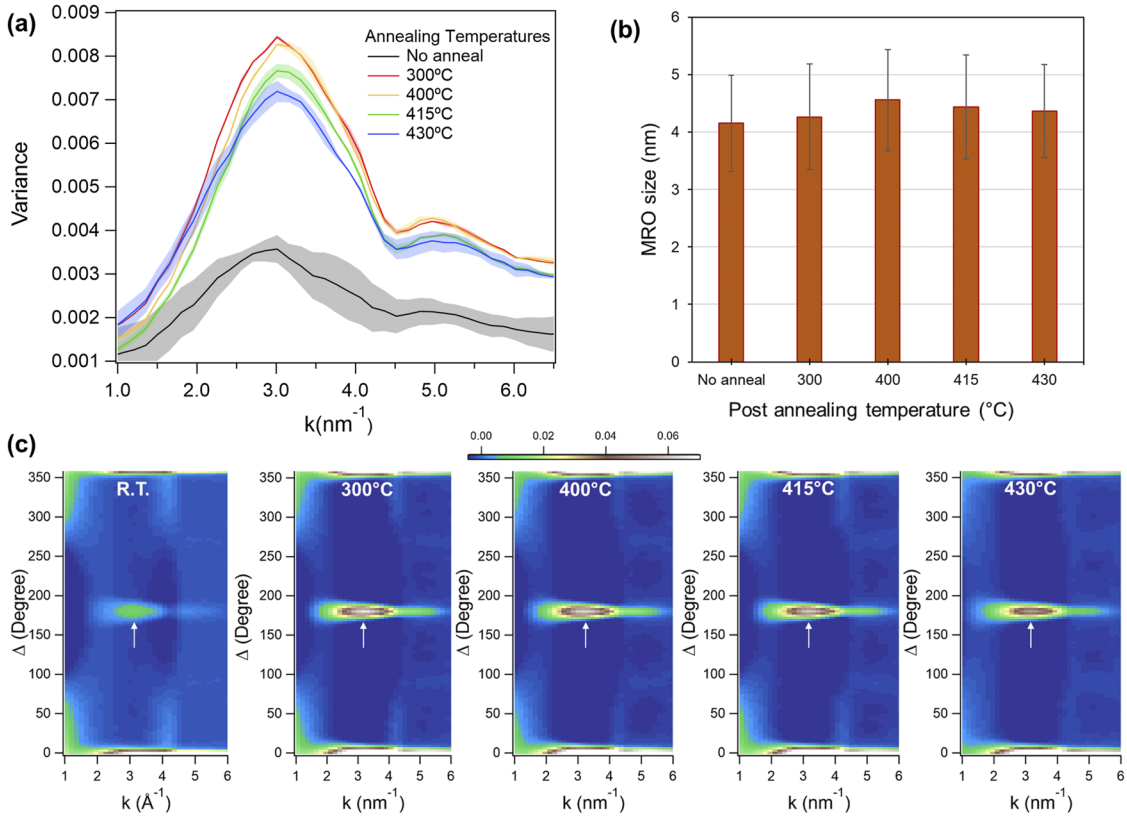

FIG. 6. (a) Intensity variance plots of the a-TiO_2 film as a function of *in situ* annealing temperatures. The shades indicate the experimental uncertainty of the measurement. The original sample was grown at 80 °C in ALD. (b) Averaged MRO size at $k \sim 3.3$ nm^{-1} for films annealed at different temperatures. (c) Averaged angular correlation function, $C_k(\Delta)$, of the a-TiO_2 films annealed at different temperatures.

positions in Fig. 3(a) changed as the growth temperature increased (first peak from ~3 to 3.3 nm^{-1} and the second peak from ~5 to 5.3 nm^{-1}). However, such peak shifting was not observed in Fig. 6(a); the peak positions remained mostly at the same positions (first peak at ~3 nm^{-1} and second peak at ~ 5 nm^{-1}). This indicates that, unlike in the case of the growth temperature study, there is no change in the overall interplanar spacing within the MRO when the degree of MRO increases upon post-annealing. In other words, this may suggest that the MRO regions (at least most of them) do not fully develop the planar ordering that eventually leads to crystallization during annealing, which is also consistent with the limited number of nucleation seen in these films when annealed [Fig. 5(g)]. The difference between the two MRO evolution (in growth vs annealing) suggests that there may be some structural features determined during low temperature growth, for example, the amount of free volume[62] or overall density of the film, that prevent the film from fully developing the crystallographic planes even when annealed at higher temperatures.

Figure 6(a) also shows that, after the crystallization starts to occur at 415 °C [which corresponds to Fig. 5(d)], the remaining amorphous region of the sample shows decreased V (green line in Fig. 6). V decreases even further when annealed at 430 °C (blue line in Fig. 6). Similar decrease in V was shown in Fig. 3 (growth temperature 140 °C vs 160 °C), which we attributed to the fact that the V was calculated from the area that were not crystallized (in other words, it was related to the spatial sampling during the 4D-STEM acquisition). However, we want to emphasize that the decrease in V at 415 °C and 430 °C in Fig. 6 is not due to spatial sampling because, as mentioned earlier, the number density of crystalline phases was very small at these temperatures and the remaining volume of the sample was still more than large enough to represent the overall structure. Therefore, we believe the decrease in V at 415 °C and 430 °C is related to the actual structural change within MRO or, more specifically, the structural relaxation of MRO at those temperatures. Structural relaxation is a well-known characteristic of amorphous materials and glasses in general[63,64] and the relationship between MRO and structural relaxation via annealing was also studied in amorphous Si and Ge[65,66] as well as metals.[33] In amorphous metals, for example, the change in structural ordering from "crystal-like" to "icosahedral-like" was suggested as a possible mechanism of MRO evolution during relaxation.[33] Similarly, in a-TiO_2, we speculate that the relaxation may involve rearrangement of polyhedrons in such ways that it relaxes the local configurational energy or minimize free volumes between the atoms (or MRO clusters).

As mentioned above, since the relaxation of MRO was observed simultaneously along with the development of MRO into crystalline nuclei, it can be suggested that some MRO regions evolve into crystals, while others become structurally relaxed. This may be related to the critical size of nuclei, meaning MRO with a certain size and higher internal ordering may have a higher likelihood of developing into crystal nuclei, while MROs that are smaller tend to be structurally relaxed (i.e., lower degree of internal ordering) when annealed. This proposed relationship between MRO and critical size of nuclei raises an important question as to the the size (or size distribution) of MRO within the film. Hence, we directly calculated the MRO size the dark field images reconstructed from the 4D-STEM data. The measured MRO size, average ± standard deviation, at k ~3.3 nm^{-1} is plotted in Fig. 6(b) for the films annealed at different temperatures. Although the measured MRO size can be overestimated since it convolutes the probe size,[34] there is a noticeable trend in MRO size shown in Fig. 6(b).[34] The MRO size increases, reaches a maximum at 400 °C (prior to crystallization), and then decreases at 415 °C and even more at 430 °C. We acknowledge that the statistical significance of this trend is not very high, as the range of error bars (standard deviation) does not clearly distinguish one bar from the others. However, the fact that the trend in Fig. 6(b) is consistent with the trend shown in $V(k)$ in Fig. 6(a) suggests that the trend observed in Fig. 6(b) is likely real, although further confirmation will be necessary by sampling MRO sizes from larger areas of the film in a future study. Assuming that the trend in Fig. 6(b) is real, the maximum size of MRO at 400 °C could be related to the critical size of crystalline nuclei. The decrease in MRO size observed at 415 °C and 430 °C can be related to the aforementioned structural relaxation.

The changes in structural symmetry of MRO within films annealed at different temperatures were studied using angular correlation function shown in Fig. 6(c). Similar to the case of growth temperature study in Fig. 3(c), all of the averaged $C_k(\Delta)$ have a hotspot at $\Delta \sim 180°$ and $k \sim 3.3\ nm^{-1}$ (white arrows), suggesting that the MRO domains have dominant 2-fold symmetry in their internal atomic arrangements and the k position of the 2-fold symmetry corresponds to the position of peaks in $V(k)$ in Fig. 6(a). Figure 6(c) shows that the intensity (color scale) of the 2-fold hotspot is initially low at room temperature, but it substantially increases at 300 °C and reaches maximum at 400 °C, a trend that is consistent with that seen for $V(k)$ in Fig. 6(a) as well as for MRO size in Fig. 6(b), which suggests enhanced atomic ordering within the MRO by annealing. The 2-fold peaks at 415 °C and 430 °C show a decrease in intensity, which indicates that the structural relaxation that occurs above 400 °C [which we already observed in $V(k)$ and MRO size] involves decrease in 2-fold ordering. This may indicate that the degree of connection between Ti–O polyhedrons (which tend to have planar alignment with 2-fold symmetry) within the MRO decreases, and this also reduces the size of the MRO during the relaxation.

IV. SUMMARY

Our work shows the detailed effects of ALD growth temperature as well as post-growth annealing temperature on the evolution of medium range ordering that directly correlates with crystallization and structural relaxation of a-TiO_2 films. Intensity variance and angular correlation analyses of nano-diffractions acquired by 4D-STEM revealed the dominant MRO type and symmetry in these films. Crystalline phase nucleates from amorphous matrix while variance is at its highest, suggesting that the regions with high degree of MRO are likely the sites for nucleation. *In situ* annealing revealed further evidence of crystallization from regions with high degree of MRO as well as the structural relaxation of MRO that are likely related to the critical size of nuclei. Crystallographic defects were observed in the nucleated crystal phases, which could adversely affect film protection during PEC performance. The work here highlights the importance of understanding and control of MRO for optimizing the structure and properties of ALD-grown amorphous films and provides practical guidance on preventing nucleation of crystal phases that could negatively impact film properties.

SUPPLEMENTARY MATERIAL

Fig. S1 in the supplementary material shows schematics of TiO_2 crystal structures, brookite, anatase, and rutile and Fig. S2 in the supplementary material shows the cross-sectional STEM image of amorphous TiO_2 film including crystalline particles.

ACKNOWLEDGMENTS

This research was primarily supported by the U.S. Department of Energy, Office of Science, Basic Energy Sciences under Award No. DE-SC0020283. Electron microscopy was performed at the Center for Electron Microscopy and Analysis at the Ohio State University.

AUTHOR DECLARATIONS

Conflict of Interest

The authors have no conflicts to disclose.

Author Contributions

Mehrdad Abbasi: Data curation (lead); Formal analysis (lead); Investigation (equal); Writing – original draft (equal). **Yutao Dong**: Data curation (equal); Formal analysis (equal); Investigation (equal); Writing – original draft (equal). **Jun Meng**: Data curation (equal); Formal analysis (equal); Writing – original draft (equal). **Dane Morgan**: Conceptualization (equal); Funding acquisition (equal); Project administration (equal); Supervision (equal); Writing – review & editing (supporting). **Xudong Wang**: Conceptualization (equal); Funding acquisition (lead); Project administration (lead); Supervision (equal); Writing – review & editing (supporting). **Jinwoo Hwang**: Conceptualization (lead); Funding acquisition (equal); Investigation (equal); Methodology (equal); Project administration (equal); Resources (equal); Software (equal); Supervision (lead); Validation (equal); Visualization (equal); Writing – original draft (equal); Writing – review & editing (lead).

DATA AVAILABILITY

The data that support the findings of this study are available from the corresponding authors upon reasonable request.

REFERENCES

[1] N. S. Lewis and D. G. Nocera, "Powering the planet: Chemical challenges in solar energy utilization," Proc. Natl. Acad. Sci. U. S. A. **103**(43), 15729–15735 (2006).
[2] N. S. Lewis, "Research opportunities to advance solar energy utilization," Science **351**, aad1920 (2016).
[3] M. G. Walter *et al.*, "Solar water splitting cells," Chem. Rev. **110**(11), 6446–6473 (2010).
[4] A. Fujishima and K. Honda, "Electrochemical photolysis of water at a semiconductor electrode," Nature **238**(5358), 37–38 (1972).
[5] A. J. Bard, "Photoelectrochemistry," Adv. Sci. **207**(4427), 139–144 (1980).
[6] A. J. Bard, "Design of semiconductor photoelectrochemical systems for solar energy conversion," J. Phys. Chem. **86**(2), 172–177 (1982).
[7] B. Turan, J. P. Becker, F. Urbain, F. Finger, U. Rau, and S. Haas, "Upscaling of integrated photoelectrochemical water-splitting devices to large areas," Nat. Commun. **7**, 12681 (2016).
[8] S. C. Warren *et al.*, "Identifying champion nanostructures for solar water-splitting," Nat. Mater. **12**(9), 842–849 (2013).
[9] Y. Zhao *et al.*, "Oxidatively stable nanoporous silicon photocathodes with enhanced onset voltage for photoelectrochemical proton reduction," Nano Lett. **15**(4), 2517–2525 (2015).
[10] K. Sun, X. Pang, S. Shen, X. Qian, J. S. Cheung, and D. Wang, "Metal oxide composite enabled nanotextured Si photoanode for efficient solar driven water oxidation," Nano Lett. **13**(5), 2064–2072 (2013).
[11] J. Oh, H. C. Yuan, and H. M. Branz, "An 18.2%-efficient black-silicon solar cell achieved through control of carrier recombination in nanostructures," Nat. Nanotechnol. **7**(11), 743–748 (2012).
[12] S. Hu, M. R. Shaner, J. A. Beardslee, M. Lichterman, B. S. Brunschwig, and N. S. Lewis, "Amorphous TiO_2 coatings stabilize Si, GaAs, and GaP photoanodes for efficient water oxidation," Science **344**(6187), 1005–1009 (2014).
[13] T. Wang, Z. Luo, C. Li, and J. Gong, "Controllable fabrication of nanostructured materials for photoelectrochemical water splitting via atomic layer deposition," Chem. Soc. Rev. **43**(22), 7469–7484 (2014).
[14] C. Zhou, Z. Xi, D. J. Stacchiola, and M. Liu, "Application of ultrathin TiO_2 layers in solar energy conversion devices," Energy Sci. Eng. **10**(5), 1614–1629 (2022).
[15] M. Liu, C.-Y. Nam, C. T. Black, J. Kamcev, and L. Zhang, "Enhancing water splitting activity and chemical stability of zinc oxide nanowire photoanodes with ultrathin titania shells," J. Phys. Chem. C **117**(26), 13396–13402 (2013).
[16] M. Leskelä and M. Ritala, "Atomic layer deposition (ALD): From precursors to thin film structures," Thin Solid Films **409**(1), 138–146 (2002).
[17] J. D. Ferguson, A. R. Yoder, A. W. Weimer, and S. M. George, "TiO_2 atomic layer deposition on ZrO_2 particles using alternating exposures of $TiCl_4$ and H_2O," Appl. Surf. Sci. **226**(4), 393–404 (2004).
[18] J. Aarik, A. Aidla, H. Mändar, and T. Uustare, "Atomic layer deposition of titanium dioxide from $TiCl_4$ and H_2O: Investigation of growth mechanism," Appl. Surf. Sci. **172**(1–2), 148–158 (2001).
[19] W. Gu and C. P. Tripp, "Role of water in the atomic layer deposition of TiO_2 on SiO_2," Langmuir **21**(1), 211–216 (2005).
[20] Z. Hu and C. H. Turner, "Initial surface reactions of TiO_2 atomic layer deposition onto SiO_2 surfaces: Density functional theory calculations," J. Phys. Chem. B **110**(16), 8337–8347 (2006).
[21] J. Leem *et al.*, "Role of HCl in atomic layer deposition of TiO_2 thin films from titanium tetrachloride and water," Bull. Korean Chem. Soc. **35**(4), 1195–1201 (2014).
[22] A. C. Bronneberg, C. Höhn, and R. Van De Krol, "Probing the interfacial chemistry of ultrathin ALD-grown TiO_2 films: An in-line XPS study," J. Phys. Chem. C **121**(10), 5531–5538 (2017).
[23] H.-E. Cheng, C.-M. Hsu, and Y.-C. Chen, "Substrate materials and deposition temperature dependent growth characteristics and photocatalytic properties of ALD TiO_2 films," J. Electrochem. Soc. **156**(8), D275 (2009).
[24] J. A. Benavides, C. P. Trudeau, L. F. Gerlein, and S. G. Cloutier, "Laser selective photoactivation of amorphous TiO_2 films to anatase and/or rutile crystalline phases," ACS Appl. Energy Mater. **1**(8), 3607–3613 (2018).
[25] Y. Yu *et al.*, "Metastable intermediates in amorphous titanium oxide: A hidden role leading to ultra-stable photoanode protection," Nano Lett. **18**(8), 5335–5342 (2018).
[26] C. Ros, N. M. Carretero, J. David, J. Arbiol, T. Andreu, and J. R. Morante, "Insight into the degradation mechanisms of atomic layer deposited TiO_2 as photoanode protective layer," ACS Appl. Mater. Interfaces **11**(33), 29725–29735 (2019).
[27] H. Zhang and J. F. Banfield, "Understanding polymorphic phase transformation behavior during growth of nanocrystalline aggregates: Insights from TiO_2," J. Phys. Chem. B **104**(15), 3481–3487 (2000).
[28] H. Zhang and J. F. Banfield, "Kinetics of crystallization and crystal growth of nanocrystalline anatase in nanometer-sized amorphous titania," Chem. Mater. **14**, 4145–4154 (2002).
[29] B. Xia, H. Huang, and Y. Xie, "Heat treatment on TiO_2 nanoparticles prepared by vapor-phase hydrolysis," Mater. Sci. Eng.: B **57**, 150–154 (1999).
[30] J. Shi, Z. Li, A. Kvit, S. Krylyuk, A. V. Davydov, and X. Wang, "Electron microscopy observation of TiO_2 nanocrystal evolution in high-temperature atomic layer deposition," Nano Lett. **13**(11), 5727–5734 (2013).
[31] J. Hwang, A. M. Clausen, H. Cao, and P. M. Voyles, "Reverse Monte Carlo structural model for a zirconium-based metallic glass incorporating fluctuation microscopy medium-range order data," J. Mater. Res. **24**(10), 3121–3129 (2009).
[32] J. M. Cowley, "Electron nanodiffraction methods for measuring medium-range order," Ultramicroscopy **90**(2–3), 197–206 (2002).
[33] J. Hwang *et al.*, "Nanoscale structure and structural relaxation in $Zr_{50}Cu_{45}Al_5$ bulk metallic glass," Phys. Rev. Lett. **108**(19), 195505 (2012).
[34] S. Im *et al.*, "Medium-range ordering, structural heterogeneity, and their influence on properties of Zr-Cu-Co-Al metallic glasses," Phys. Rev. Mater. **5**(11), 115604 (2021).
[35] M. M. J. Treacy, J. M. Gibson, L. Fan, D. J. Paterson, and I. McNulty, "Fluctuation microscopy: A probe of medium range order," Rep. Prog. Phys. **68**(12), 2899–2944 (2005).
[36] P. M. Voyles and D. A. Muller, "Fluctuation microscopy in the STEM," Ultramicroscopy **93**(93), 147–159 (2002).
[37] P. M. Voyles and J. R. Abelson, "Medium-range order in amorphous silicon measured by fluctuation electron microscopy," Sol. Energy Mater. Sol. Cells **78**(1–4), 85–113 (2003).
[38] B. Lee, "Observation of the role of subcritical nuclei in crystallization of a glassy solid," Science **326**(November), 980–984 (2009).
[39] A. Rezikyan and G. G. Moore, "Fluctuation electron microscopy study of crystal nucleation in TiO_2- SiO_2 glass with heat treatment," J. Phys.: Condens. Matter **32**, 485402 (2020).
[40] P. Wochner *et al.*, "X-ray cross correlation analysis uncovers hidden local symmetries in disordered matter," Proc. Natl. Acad. Sci. U. S. A. **106**(28), 11511–11514 (2009).
[41] A. C. Y. Liu *et al.*, "Systematic mapping of icosahedral short-range order in a melt-spun $Zr_{36}Cu_{64}$ metallic glass," Phys. Rev. Lett. **110**(20), 205505 (2013).
[42] M. Altarelli, R. P. Kurta, and I. A. Vartanyants, "X-ray cross-correlation analysis and local symmetries of disordered systems: General theory," Phys. Rev. B: Condens. Matter Mater. Phys. **82**(10), 104207 (2010).
[43] C.-P. Lin, H. Chen, A. Nakaruk, P. Koshy, and C. C. Sorrell, "Effect of annealing temperature on the photocatalytic activity of TiO_2 thin films," Energy Procedia **34**, 627–636 (2013).
[44] M. W. Tate *et al.*, "High dynamic range pixel array detector for scanning transmission electron microscopy," Microsc. Microanal. **22**(1), 237–249 (2016).
[45] J. M. Gibson, M. M. J. Treacy, and P. M. Voyles, "Atom pair persistence in disordered materials from fluctuation microscopy," Ultramicroscopy **83**(3–4), 169–178 (2000).
[46] H. P. Klug and L. E. Alexander, X-ray diffraction procedures: for polycrystalline and amorphous materials, 1974.
[47] J. E. Gerbi, P. M. Voyles, M. M. J. Treacy, J. M. Gibson, and J. R. Abelson, "Increasing medium-range order in amorphous silicon with low-energy ion bombardment," Appl. Phys. Lett. **82**(21), 3665–3667 (2003).
[48] J. Hwang and P. M. Voyles, "Variable resolution fluctuation electron microscopy on Cu-Zr metallic glass using a wide range of coherent STEM probe size," Microsc. Microanal. **17**, 67–74 (2011).
[49] T. Sun, M. M. J. Treacy, T. Li, N. J. Zaluzec, and J. M. Gibson, "The importance of averaging to interpret electron correlographs of disordered materials," Microsc. Microanal. **20**(2), 627–634 (2014).

[50]E. D. Bøjesen, T. C. Petersen, A. V. Martin, M. Weyland, and A. C. Y. Liu, "Statistical measures of angular correlations in amorphous materials from electron nano-diffraction in the scanning/transmission electron microscope," J. Phys. Mater. **3**(4), 044002 (2020).
[51]S. Im *et al.*, "Direct determination of structural heterogeneity in metallic glasses using four-dimensional scanning transmission electron microscopy," Ultramicroscopy **195**(September), 189–193 (2018).
[52]J. Taylor, Introduction to error analysis, the study of uncertainties in physical measurements, 1997.
[53]M. Horn, C. F. Schwerdtfeger, and E. P. Meagher, "Refinement of the structure of anatase at several temperatures," Z. Krist. **136**(3–4), 273–281 (1972).
[54]E. P. Meagher and G. A. Lager, "Polyhedral thermal expansion in the TiO_2 polymorphs; refinement of the crystal structures of rutile and brookite at high temperature," Can. Mineral. **17**(1), 77–85 (1979).
[55]K. Sugiyama and Y. Takéuchi, "The crystal structure of rutile as a function of temperature up to 1600°C," Z. Krist. - Cryst. Mater. **194**(3–4), 305–313 (1991).
[56]C. Hu *et al.*, "A multi-method study of the transformation of the carbonaceous skeleton of a polymer-based nanoporous carbon along the activation pathway," Carbon **85**, 119–134 (2015).
[57]M. M. J. Treacy and K. B. Borisenko, "The local structure of amorphous silicon," Science **335**(6071), 950–953 (2012).
[58]M.-Y. Ho *et al.*, "Morphology and crystallization kinetics in HfO_2 thin films grown by atomic layer deposition," J. Appl. Phys. **93**(3), 1477–1481 (2003).
[59]J. Mavračić, F. C. Mocanu, V. L. Deringer, G. Gábor, C. Csányi, and S. R. Elliott, "Similarity between amorphous and crystalline phases: The case of TiO_2," J. Phys. Chem. Lett. **9**, 53 (2018).
[60]K. Yang *et al.*, "New insights into the atomic structure of amorphous TiO_2 using tight-binding molecular dynamics," J. Chem. Phys. **149**(9), 094501 (2018).
[61]V. Petkov, G. Holzhüter, U. Tröge, T. Gerber, and B. Himmel, "Atomic-scale structure of amorphous TiO_2 by electron, X-ray diffraction and reverse Monte Carlo simulations," J. Non-Cryst. Solids **231**(1–2), 17–30 (1998).
[62]D. Turnbull and M. H. Cohen, "Free-volume model of the amorphous phase: Glass transition," J. Chem. Phys. **34**(1), 120–125 (1961).
[63]F. H. Stillinger, "Relaxation and flow mechanisms in 'fragile' glass-forming liquids," J. Chem. Phys. **89**(10), 6461–6469 (1988).
[64]C. A. Angell, "Spectroscopy simulation and scattering, and the medium range order problem in glass," J. Non-Cryst. Solids **73**(1–3), 1–17 (1985).
[65]J.-Y. Cheng, J. M. Gibson, and D. C. Jacobson, "Observations of structural order in ion-implanted amorphous silicon," J. Mater. Res. **16**(11), 3030–3033 (2001).
[66]J. M. Gibson and M. M. J. Treacy, "Diminished medium-range order observed in annealed amorphous germanium," Phys. Rev. Lett. **78**(6), 1074 (1997).